Autonomous Navigation Using Integrated X-ray Pulsar and Optical Measurements

Sui Chen[(1)] and Francesco Topputo[(2)]

[(1)]*Department of Aerospace Science and Technology, Politecnico di Milano*
Via La Masa 34, 20156, Milan, Italy
sui.chen@polimi.it

[(2)] *Department of Aerospace Science and Technology, Politecnico di Milano*
Via La Masa 34, 20156, Milan, Italy
francesco.topputo@polimi.it

***Abstract* – In light of several constraints inherent in ground-based navigation systems for space missions, this work introduces a novel concept of an autonomous integrated navigation system combining X-ray pulsar and optical measurements. Deep-space navigation scenarios are addressed where the spacecraft lacks proximity to any planetary body. A hypothetical 4-hour navigation cycle is assessed which consists of solely optical navigation and integrated pulsar and optical navigation. An extended Kalman filter (EKF) is implemented for spacecraft state estimation. Simulation results indicate that integrating X-ray pulsar measurements with optical measurements significantly improves the navigation accuracy compared to conventional optical navigation, yielding position errors below 3 km. This study highlights the potential for realising fully autonomous deep-space navigation with high accuracy, which is deemed a future trend in space missions.**

I. INTRODUCTION

Recent technological advancement and the expanding commercial landscape in the space sector have led to a significant surge in the development of space exploration missions. Presently, space mission operation relies heavily on ground-based Guidance, Navigation and Control (GNC) systems, often requiring human intervention. Although reliable, this approach is not without its limitations. Communication latency, lack of read-time responsiveness, and the challenge of potential ground infrastructure saturation due to the escalating growth of space users underscore the need for innovative solutions. To mitigate these challenges, there is a growing emphasis on developing onboard autonomous navigation techniques. This shift aims to reduce dependency on ground-based operations, offering a potential solution for future space missions.

Extensive research has been conducted on various autonomous navigation technologies. Of all the techniques being studied and proposed, optical navigation (OPNAV) stands out as one of the most mature. Numerous research works exist regarding the conceptual framework and implementation of optical navigation [1] [2] [3] [4]. In principle, spacecraft orbits are determined through onboard imaging, which measures the inertial direction from the spacecraft to target bodies. In scenarios involving deep space far-range navigation, the observed target bodies typically appear as unresolved, small bright dots in the captured images. The measurement information is therefore the line-of-sight (LoS) directions to these target bodies, which are subsequently fed into an orbit determination algorithm to estimate the spacecraft's state. Several missions have undertaken in-flight demonstrations to test the concepts of deep space optical navigation. As part of NASA's New Millennium Program, Deep Space 1 [5] was the first mission to validate the concept of an autonomous onboard navigation system, utilising images of several distant asteroids to determine the spacecraft's trajectory. More recently, the Lunar Flashlight mission [6] conducted an optical navigation experiment incorporating a star tracker, marking the first on-orbit demonstration of heliocentric navigation relying solely on optical observations of planets. However, it is noteworthy that the navigation accuracy attained through optical navigation typically falls short compared to other navigation methods [7], resulting in position uncertainties that often accumulate to several thousand kilometres [8]. For missions that require precise pointing or spacecraft docking, a more accurate navigation solution becomes essential.

An alternative and highly attractive method for autonomous spacecraft navigation is X-ray pulsar navigation (XNAV) which relies on pulsar timing. Pulsars are fast-rotating neutron stars that emit stable, periodic and predictable signals characterised by unique shapes. These features enable pulsar-based navigation to achieve extremely high accuracy. In particular, X-ray pulsars are often preferred for navigation among different electromagnetic bands due to their higher signal-to-noise ratio, allowing for the use of smaller and lighter detectors compared to optical or radio sources [9]. The concept of leveraging these celestial sources as a navigation tool traces back to the 1970s, when Downs [10] explored the potential of utilising pulsating radio sources for interplanetary navigation. Essentially, the pulse time of arrivals (TOAs) measured onboard of a spacecraft are utilised to estimate the spacecraft's state.

In 2016, XPNAV-1 [11] was launched to conduct a ground pulsar-based navigation experiment, utilising pulsar observation data collected onboard. This experiment resulted in an average navigation accuracy of 38.4 km solely through observations of the Crab pulsar. In 2017, NASA demonstrated a fully autonomous, real-time pulsar navigation experiment in space for the first time, attaining an average accuracy of 16 km [12] [13].

While theoretically highly accurate, pulsar-based navigation currently possesses a low technological readiness level and has not reached a sufficient level of maturity to serve as the sole method for autonomous navigation systems. Given the comparatively advanced stage of development of optical navigation, it seems sensible to explore the potential benefits of integrating these two techniques as complementary to each other.

In fact, some existing literature already attempted to address integrated navigation systems. Xiong et al. 2016 [14] integrated an ultraviolet optical sensor into an XNAV system to provide preliminary orbit estimates, effectively improving the navigation accuracy of the system. Ning et al. 2017 [15] introduced a differential X-ray pulsar-aided celestial navigation system integrating measurements of star angles and pulse times of arrival. This approach led to enhancements in both system robustness and navigation accuracy. Gu et al. 2019 [16] proposed an integrated navigation system that combines optical, radio, and X-ray pulsar measurements to improve navigation accuracy and to fully satisfy the requirements of a Mars orbiter. Zhang et al. 2022 [17] introduced a ranging-enhanced XNAV method. It involves substituting one X-ray pulsar with a satellite to provide one-dimensional ranging information, which was integrated with pulse TOAs from two other pulsars. This proposed system demonstrated a 70% increase in position accuracy compared to the conventional XNAV based on three pulsars.

Among the aforementioned work on integrated autonomous navigation systems, most of them have dealt with mid-range or close-range scenarios when it comes to optical navigation where the target bodies' dimensions and features are visible and can be resolved. Little work has been dedicated to dealing with deep-space scenarios where the spacecraft is not in the vicinity of any planets or asteroids, which is typically the case in deep-space scenarios. This paper will therefore focus on developing an integrated autonomous navigation system that incorporates optical and X-ray pulsar measurements in deep-space scenarios. Given a hypothetical navigation scenario, the proposed integrated system performance will be evaluated through numerical simulations.

The rest of this paper is structured as follows. Section II describes the spacecraft dynamics and measurement models necessary for an integrated navigation system. Section III provides an overview of the simulation settings and the navigation scenario, followed by the simulation results. Lastly, Section IV concludes the paper.

II. METHODOLOGY

A. Dynamics

For a deep-space interplanetary spacecraft, its dynamics can be described using the following equation:

$$\dot{\mathbf{x}}(t) = \boldsymbol{f}(\mathbf{x}(t), t) + \boldsymbol{w} \tag{1}$$

where $\mathbf{x}$ is the process state comprising of spacecraft position and velocity $\mathbf{x}(t) = [\mathbf{r}(t), \mathbf{v}(t)]^{\mathrm{T}}$, $\boldsymbol{w}$ is the process white noise and $\boldsymbol{f}$ is defined as:

$$\boldsymbol{f} = \begin{bmatrix} \mathbf{v} \\ -\mu_{\mathrm{Sun}} \dfrac{\mathbf{r}}{\mathrm{r}^3} + \mathbf{a}_{\mathrm{pert}} \end{bmatrix} \tag{2}$$

For an interplanetary spacecraft, the main perturbation acceleration $\boldsymbol{a}_{\mathrm{pert}}$ consists of solar radiation pressure and third-body perturbation from other planets in the solar system:

$$\mathbf{a}_{\mathrm{pert}} = \mathbf{a}_{\mathrm{SRP}} + \mathbf{a}_{\mathrm{3rd}} \tag{3}$$

where

$$\mathbf{a}_{\mathrm{SRP}} = \frac{S}{c}\left(\frac{D_{AU}}{\mathrm{r}}\right)^2 C_R \frac{A_s}{m} \frac{\mathbf{r}}{\mathrm{r}}$$

$$\mathbf{a}_{\mathrm{3rd}} = \sum_{\mathrm{i}} \mathbf{a}_{\mathrm{pl_i}} = \sum_{\mathrm{i}} \mu_{\mathrm{pl_i}} \left(\frac{\mathbf{r}_{\mathrm{pl_i}} - \mathbf{r}}{\left\| \mathbf{r}_{\mathrm{pl_i}} - \mathbf{r} \right\|^3} - \frac{\mathbf{r}_{\mathrm{pl_i}}}{\left\| \mathbf{r}_{\mathrm{pl_i}} \right\|^3} \right)$$

In the above equations, S is the power intensity at 1 Astronomical Unit (AU) and has a value of 1367 W/m^2, c is the speed of light, D_{AU} is the distance of 1 AU equal to 149.6×10^6 km, C_R is the spacecraft reflectivity coefficient, A_s is the satellite exposed area to the Sun and m is the spacecraft mass.

B. X-ray pulsar measurement

For each pulsar observed, the signal is detected as the pulse photons collected at the X-ray detector onboard of the spacecraft. The fundamental measurement for XNAV is the photon time of arrivals (TOAs). The complete pipeline of signal processing goes as follows. First, the photon TOA timestamps are collected at the spacecraft. These TOAs are subsequently transferred from the moving spacecraft to an inertial point in space, usually the solar system barycentre (SSB). These TOAs are folded into one pulse period using the epoch folding technique to create an observed pulse profile. A standard

pulse profile is constructed based on the pulse shape function and the estimated spacecraft position. Following that, a nonlinear least square (NLS) technique is used to compare the observed profile with the standard pulse profile to obtain the phase shift between them. This phase shift will correspond to the distance shift between the true spacecraft position and the estimated spacecraft position projected along the line of sight of the pulsar. The results are then fed into a navigation filter for spacecraft state estimation and correction.

Fig. 1. provides a geometrical illustration of the spacecraft position in relation to the SSB and spacecraft range along the direction of a pulsar line of sight. Given the substantial distance of the pulsar from the solar system, it is assumed that the direction of the pulsar remains constant within the solar system, i.e., $\hat{\boldsymbol{n}}_{SC} \approx \hat{\boldsymbol{n}}_{SSB} \approx \hat{\boldsymbol{n}}$. From this simple geometrical relationship and taking into account some higher-order time delay effects [18], the measurement model $\mathrm{h}(\mathbf{x})$ is defined as:

$$h_{\mathrm{pulsar}}(\mathbf{x}) = \mathrm{t_{SSB}} - \mathrm{t_{sc}} = \frac{\hat{\mathbf{n}} \cdot \mathbf{r}}{\mathrm{c}} + \frac{1}{2\mathrm{cD_0}}[(\hat{\mathbf{n}} \cdot \mathbf{r})^2 - \mathrm{r}^2 + 2(\hat{\mathbf{n}} \cdot \mathbf{b})(\hat{\mathbf{n}} \cdot \mathbf{r}) - 2(\mathbf{b} \cdot \mathbf{r})] + \frac{2\mu_{\mathrm{Sun}}}{\mathrm{c}^3} \ln\left|\frac{\hat{\mathbf{n}} \cdot \mathbf{r} + \mathrm{r}}{\hat{\mathbf{n}} \cdot \mathbf{b} + \mathrm{b}} + 1\right| \quad (4)$$

where $\hat{\mathbf{n}}$ is the unit direction vector from the SSB to the pulsar, $\mathbf{r}$ is the spacecraft position vector from the SSB, c is the speed of light, D_0 is the distance between the SSB and the pulsar, $\mathbf{b}$ is the vector from the Sun centre to the SSB and μ_{Sun} is the gravitational constant of the Sun. The first term in the right-hand side of (4) denotes the first-order *Doppler delay*, representing the direct geometric time delay between the spacecraft and the SSB. The second term arises from parallax effects, and collectively, the first two terms are named as *Roemer delay*. The last term is the Sun's *Shapiro delay*, accounting for the additional time delay resulting from curved path of light influenced by the gravitational field of the Sun. If only the first term is considered while discarding the remaining higher order terms, (4) is reduced to the simple geometrical relationship between the pulsar TOA difference and the spacecraft range along the pulsar direction as illustrated in Fig. 1.

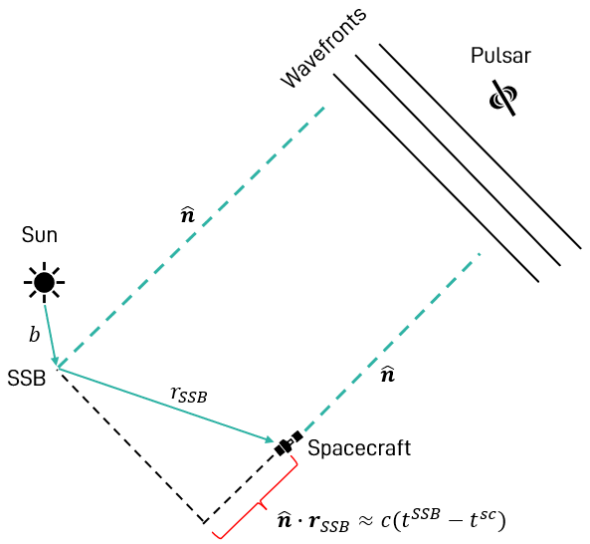

Fig. 1. Geometrical representation of the X-ray pulsar navigation.

During flight, the entire pipeline of signal processing as described above will be run within the measurement acquisition windows. In this work, we will focus primarily on studying the navigation performance, and thus the measurements are simulated directly by evaluating the measurement model with random white noise added. Photon-level TOAs generation and signal processing are not simulated in this paper. Therefore, for each discrete time stamp k, the measurements are generated as:

$$\boldsymbol{y}_{\mathrm{pulsar_k}} = h_{\mathrm{pulsar}}(\mathbf{x}_{\mathrm{k}}) + \boldsymbol{v}_{\mathrm{pulsar_k}} \quad (5)$$

The measurement noise is computed from the signal-to-noise ratio (SNR) of a specific pulsar as:

$$\sigma_{TOA} = \frac{1}{2}\frac{W}{SNR} \quad (6)$$

$$SNR = \frac{F_x A_x p_f T_{obs}}{\sqrt{\left[B_x + F_x(1 - p_f)\right]\left(A_x T_{obs}\frac{W}{P}\right) + F_x A_x p_f T_{obs}}} \quad (7)$$

where W is the pulse width, F_x is the observed X-ray photon flux, A_x is the detector area, p_f is the pulsed fraction, T_{obs} is the total observation time, B_x is the X-ray background radiation flux and P is the pulse period.

C. Optical measurement

Optical measurement information is obtained by processing images captured by an onboard navigation camera. After image processing, the spacecraft position is estimated from the detected beacon's line of sight (LoS) directions via celestial triangulation as shown in Fig. 3. This geometrical relationship is described by (8).

$$\boldsymbol{\rho} = \boldsymbol{r}_p - \boldsymbol{r} = \begin{bmatrix} x_p - x \\ y_p - y \\ z_p - z \end{bmatrix} \quad (8)$$

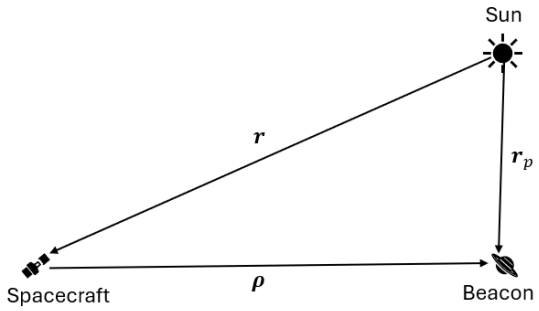

Fig. 3. Geometrical representation of celestial triangulation scheme in deep-space optical navigation.

The beacon LoS direction is represented by two angles, namely the azimuth (*Az*) and elevation (*El*), as shown in Fig. 4. From geometry, the measurement model for deep-space optical navigation is therefore defined as:

$$\boldsymbol{h}_{optical}(\mathbf{x}) = \begin{bmatrix} Az \\ El \end{bmatrix} = \begin{bmatrix} \tan^{-1}\left(\dfrac{y_p - y}{x_p - x}\right) \\ \sin^{-1}\left(\dfrac{z_p - z}{\|\boldsymbol{\rho}\|}\right) \end{bmatrix} \quad (9)$$

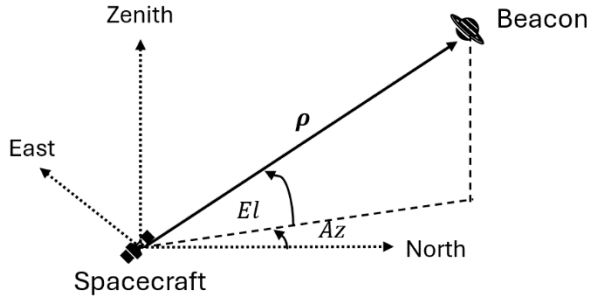

Fig. 4. The beacon line of sight (LoS) direction is defined by the angles azimuth (*Az*) and elevation (*El*).

Similar to the pulsar measurement simulation, the optical observations are directly generated by using the optical measurement model evaluated at the true spacecraft state added with measurement noise:

$$\boldsymbol{y}_{\text{optical}_\text{k}} = \boldsymbol{h}_{\text{optical}}(\mathbf{x}_\text{k}) + \boldsymbol{v}_{\text{optical}_\text{k}} \quad (10)$$

The combined navigation system integrates the pulsar and optical measurements according to (11):

$$\boldsymbol{y}_{\text{integrated}_\text{k}} = \begin{bmatrix} \boldsymbol{h}_{\text{pulsar}}(\mathbf{x}_\text{k}) \\ \boldsymbol{h}_{optical}(\mathbf{x}_\text{k}) \end{bmatrix} + \begin{bmatrix} \boldsymbol{v}_{\text{pulsar}_\text{k}} \\ \boldsymbol{v}_{\text{optical}_\text{k}} \end{bmatrix} \quad (11)$$

III. NAVIGATION SIMULATION

A. Simulation settings

A hypothetical interplanetary spacecraft between the Earth and the Mars is used in our simulation to test the proposed integrated navigation system. The spacecraft properties and its initial condition (on 01 January 2025 00:00:00) are summarised in Tables 1 and 2 respectively. The spacecraft's state is propagated using the perturbed dynamics described in Section IIA, with the third-body perturbation effects from all planets in the solar system taken into account. The resultant trajectory will be used as the *reference* or *true* trajectory for the following analysis of the navigation system performance.

Table 1. Spacecraft properties.

Mass *m* (kg)	100
Surface area A_s (m^2)	5
X-ray detector area A_x (m^2)	1
Reflectivity coefficient C_R	1.3

Table 2. Initial condition for the hypothetical interplanetary spacecraft, in the SSB inertial frame.

Position (km)		Velocity (km/s)	
x_0	1.795e+8	v_{x_0}	-6.683
y_0	1.945e+8	v_{y_0}	-1.179
z_0	-1.646e+8	v_{z_0}	10.326

The pulsar B0531+21 (Crab pulsar) has the highest SNR among all suitable pulsar sources given its large flux, large pulsed fraction, short duty cycles and narrow pulse width [18]. This would yield accurate timing and range estimates according to (6) and (7). The Crab pulsar is therefore selected as the XNAV measurement source. Its key characteristics are summarised in Table 3 [19].

Table 3. Crab pulsars' key properties [19].

Period *P* (ms)	33.4
Pulsed fraction p_f (%)	70
Flux F_x (ph $cm^{-2}s^{-1}$)	1.54
Pulse width *W* (s)	0.00167
Galactic longitude (°)	184.56
Galactic latitude (°)	-5.78
Distance D_0 (kpc)	2.00

For optical navigation, Earth and Mars are selected as the two beacons to provide their LoS measurements. An extended Kalman filter (EKF) is implemented onboard to perform real-time spacecraft state estimation. The filter blends the pulsar and optical measurements with the spacecraft dynamics model to update the spacecraft state estimate. Table 4 summarises the filter settings.

Table 4. Navigation filter settings.

Process noise q (m s^{-2})	3
Optical measurement noise $v_{optical}$ (rad)	1×10^{-5}
Pulsar measurement noise v_{pulsar} (s)	3.68×10^{-7}
Optical sensor frequency (s^{-1})	1/50
X-ray sensor frequency (s^{-1})	1/300

B. Navigation scenario

A measurement acquisition window of 3 hours is simulated. Considering the more advanced stage of maturity in optical navigation, optical measurements are acquired continuously at intervals of 50 seconds throughout the 3-hour acquisition window. In the first one hour, optical measurements are recorded from observing the Mars (1st planet). Subsequently, X-ray pulsar measurements from the Crab pulsar are added alongside the optical data for an additional hour. In the final hour of the acquisition window, the Earth (2nd planet) is observed to generate optical measurements. Following this, no measurements are taken, and the spacecraft's state is propagated for an additional hour. The four-hour navigation cycle will be repeated. The navigation scenario described above is illustrated in Fig. 5.

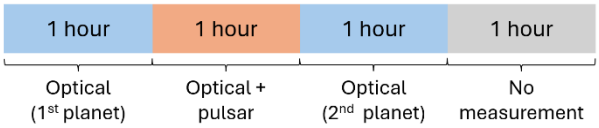

Fig. 5. One full navigation cycle which lasts for 4 hours.

C. Simulation results

A Monte Carlo simulation comprising of 15 samples is conducted for three navigation cycles with a total duration of 12 hours. Fig. 6 shows the estimation errors of spacecraft position and velocity obtained from the simulation. The black lines represent the error profiles for the 15 samples and the red lines represent the 3σ covariance bounds. Fig. 7 displays the zoomed-in plots of a segment within the acquisition window where the integrated X-ray pulsar and optical measurements are obtained.

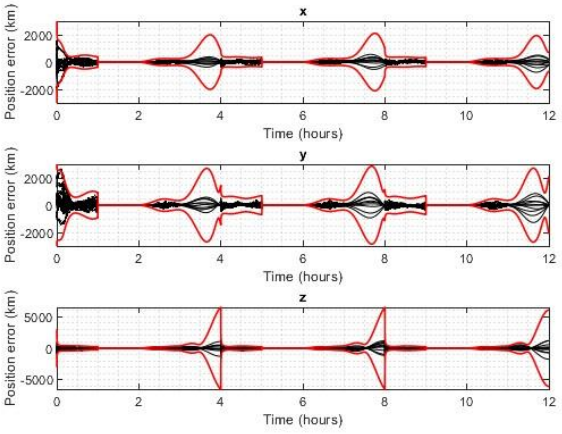

Fig. 6a. Position errors.

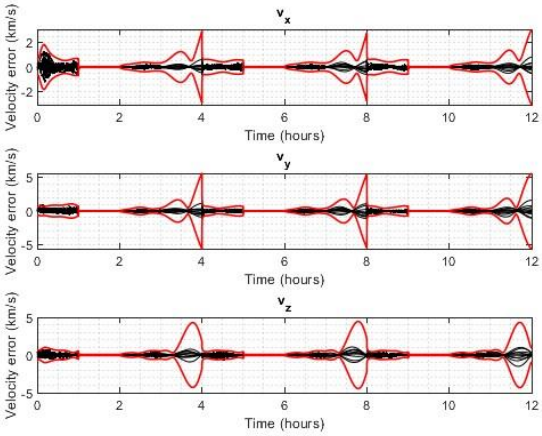

Fig. 6b. Velocity errors.

Fig. 6. Filter performance for three navigation cycles. The black lines represent the error profiles from 15 Monte Carlo samples, and the red lines represent the 3σ covariance bounds.

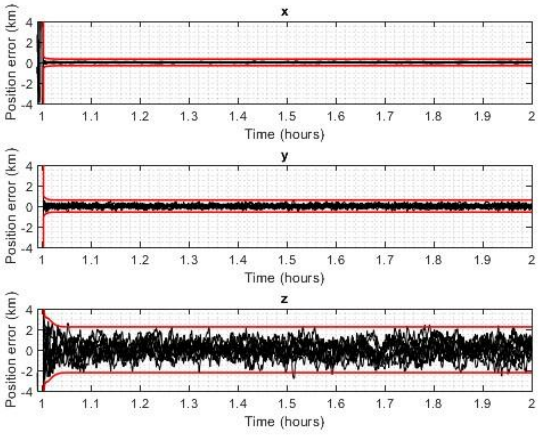

Fig. 7a. Position errors.

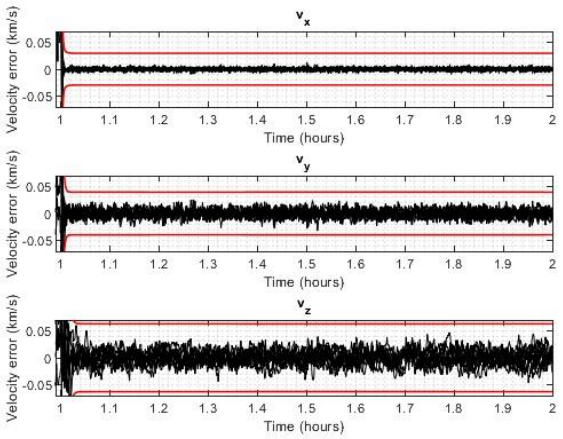

Fig. 7b. Velocity errors.

Fig. 7. Zoomed-in filter performance during an acquisition window where the integrated X-ray pulsar and optical measurements are used.

From the results, it is evident that in the absence of measurement input, the spacecraft position errors grow to the order of 10^3 km in a 1-hour timeframe. When optical measurements are available, the position errors are reduced significantly to the order to 200 km. Moreover, upon combining pulsar measurements with optical data, the proposed integrated navigation system demonstrates markedly improved accuracy, yielding position estimation errors below 3 km. Table 5 summarises the achievable accuracy of the proposed integrated navigation system.

Table 5. Navigation accuracy of the proposed integrated X-ray pulsar and optical system.

Position (km)		Velocity (km/s)	
δx	0.3128	δv_x	0.0294
δy	0.5910	δv_y	0.0395
δz	2.2307	δv_z	0.0628

The simulation results demonstrate the superior accuracy achieved by the proposed integrated navigation system which combines X-ray pulsar and optical measurement data. By integrating the more well-established optical navigation method with the less mature yet highly accurate X-ray pulsar navigation technique, this work has introduced the novel approach that caters to the demand for precise positioning in space missions as required, while concurrently maintaining a certain level of system reliability. Additionally, it has featured the capacity for attaining high accuracy even in deep-space scenarios where the spacecraft lacks proximity to planetary bodies to exploit and extract their close-up features. Considering the constraints inherent in ground-based navigation systems, this study has demonstrated the potential for realising fully autonomous spacecraft navigation, which is deemed a future trend in space missions.

IV. Conclusion

In this work, a novel concept of an integrated navigation system combining X-ray pulsar and optical measurements is proposed. Deep-space navigation scenarios are considered where the spacecraft is not in proximity to any planetary body. A hypothetical navigation cycle of 4 hours is assessed which consists of solely optical navigation and integrated pulsar and optical navigation. The measurements are fed into an EKF to estimate the spacecraft's state. The proposed navigation scheme is tested via numerical simulations. The simulation results indicate that integrating X-ray pulsar measurements with optical measurements significantly enhances the navigation accuracy compared to conventional optical navigation. This study highlights the potential for achieving fully autonomous deep-space navigation with high accuracy. Future work could explore the impact of different filtering schemes and incorporate signal processing pipelines to generate more realistic measurement data for input into the navigation filter.

V. References

[1] Gaskell, R., Barnouin-Jha, O., Scheeres, D. J., Konopliv, A., Mukai, T., Abe, S., Saito, J., Ishiguro, M., Kubota, T., Hashimoto, T., et al. "Characterizing and navigating small bodies with imaging data." *Meteoritics & Planetary Science*, Vol. 43, No. 6, pp. 1049–1061, 2008.

[2] Li, S., Lu, R., Zhang, L., and Peng, Y. "Image processing algorithms for deep-space autonomous optical navigation." *The Journal of Navigation*, Vol. 66, No. 4, pp. 605–623, 2013.

[3] Raymond Karimi, R. and Mortari, D. "Interplanetary autonomous navigation using visible planets*." Journal of Guidance, Control, and Dynamics*, Vol. 38, No. 6, pp. 1151–1156, 2015.

[4] Andreis, E., Franzese, V., Topputo, F., et al. "An overview of autonomous optical navigation for deep-space CubeSats." *International Astronautical Congress: IAC Proceedings*, pp. 1–11. 2021.

[5] Bhaskaran, S., Desai, S., Dumont, P., Kennedy, B., Null, G., Owen Jr, W., Riedel, J., Synnott, S., and Werner, R. "Orbit determination performance evaluation of the deep space 1 autonomous navigation system." 1998.

[6] Krause, M., Thrasher, A., Soni, P., Smego, L., Isaac, R., Nolan, J., Pledger, M., Lightsey, E. G., Ready, W. J., and Christian, J. "LONEStar: The Lunar Flashlight Optical Navigation Experiment." arXiv preprint arXiv:2401.12198, 2024.

[7] Turan, E., Speretta, S., and Gill, E. “Autonomous navigation for deep space small satellites: Scientific and technological advances.” *Acta Astronautica*, Vol. 193, pp. 56–74, 2022.
[8] Becker, W., Kramer, M., and Sesana, A. “Pulsar timing and its application for navigation and gravitational wave detection.” *Space Science Reviews*, Vol. 214, pp. 1–25, 2018.
[9] Cacciatore, F., Ruiz, V. G., Taubmann, G., Munoz, J., Hermosin, P., Sciarra, M., Saco, M., Rea, N., Hernanz, M., Parent, E., et al. “PODIUM: A Pulsar Navigation Unit for Science Missions.” arXiv preprint arXiv:2301.08744, 2023.
[10] Downs, G. “Interplanetary navigation using pulsating radio sources.” *Tech. rep*., 1974.
[11] Huang, L., Shuai, P., Zhang, X., and Chen, S. “Pulsar-based navigation results: data processing of the x-ray pulsar navigation-I telescope.” *Journal of Astronomical Telescopes, Instruments, and Systems*, Vol. 5, No. 1, pp. 018003–018003, 2019.
[12] Witze, A. “NASA test proves pulsars can function as a celestial GPS.” *Nature*, Vol. 553, No. 7688, pp. 261–263, 2018.
[13] Keesey, L. and Skelly, C. “NASA team first to demonstrate X-ray navigation in space.”, 2018.
[14] Xiong, K., Wei, C., and Liu, L. “Performance enhancement of X-ray pulsar navigation using autonomous optical sensor.” *Acta Astronautica*, Vol. 128, pp. 473–484, 2016.
[15] Ning, X., Gui, M., Fang, J., and Liu, G. “Differential X-ray pulsar aided celestial navigation for Mars exploration.” *Aerospace Science and Technology*, Vol. 62, pp. 36–45, 2017.
[16] Gu, L., Jiang, X., Li, S., and Li, W. “Optical/radio/pulsars integrated navigation for Mars orbiter.” *Advances in Space Research*, Vol. 63, No. 1, pp. 512–525, 2019.
[17] Zhang, L., Fang, H., Bao, W., Sun, H., Shen, L., Su, J., and Zhao, L. “Enhanced X-ray pulsar navigation based on ranging information of a satellite.” *Aircraft Engineering and Aerospace Technology*, Vol. 94, No. 10, pp. 1872–1882, 2022.
[18] Sheikh, S. I. “The use of variable celestial X-ray sources for spacecraft navigation.” *University of Maryland*, College Park, 2005.
[19] Becker, W. and Trumper, J. “The X-ray luminosity of rotation-powered neutron stars.” *Astronomy and Astrophysics*, Vol. 326, October 1997, pp. 682-691.